Electronic Supplementary Information

Renovating Surface Matrix of $FAPbI_3$ Perovskite Quantum Dots *via* Phase-transfer Catalysis for 16.29% Efficiency Solar Cells

Mingxu Zhang,[a] Qiyuan Gao,[a] Xinyi Mei,[a] Junming Qiu,[a] Rongshan Zhuang,[b] Yong Hua,[b] Zhimei Sun,[a]* and Xiaoliang Zhang [a]*

[a] School of Materials Science and Engineering, Beihang University, Beijing 100191, China

[b] Yunnan Key Laboratory for Micro/Nano Materials & Technology, School of Materials and Energy, Yunnan University, Kunming 650091, China

*Correspondence author E-mail address: zmsun@buaa.edu.cn (Z. Sun); xiaoliang.zhang@buaa.edu.cn（X. Zhang）

Supporting Information Contents

Note S1: The universality of the phase transfer catalysis strategy.

Experimental Section

Materials:

All reagents were used as received without further purification. Octadecene (ODE, >90%(GC)), oleic acid (OA, technical grade 90%), oleylamine (OAm, technical grade 80-90%), n-hexane (>99% (GC)), n-octane (>99% (GC)), methyl acetate (MeOAc, anhydrous 99.5%) and ethyl acetate (EtOAc, spectrographic grade 99.5%) were purchased from Aladdin. 3-(Trifluoromethyl) phenyltrimethylammonium (3-CF_3-PTAI) iodide was purchased from Boer. Formamidine acetate (FAAc, >98.0%(T)), and methylammonium iodide (MAI, 99.0%) were purchased from TCI. 2-pentanol (2-PeOH, 99%), SnO_2 (15% in H_2O colloidal dispersion) were purchased from Alfa Aesar. Formamidinium iodide (FAI, ≥99.5%), lead iodide (PbI_2, 99%), 2,2′,7,7′-tetrakis (N,Ndi-p-methoxyphenylamine)-9,9′spirobifluorene (spiro-OMeTAD, ≥99.5%) and tris(2-(1Hpyrazol-1-yl)-4-tert-butylpyridine)-cobalt(III)Tris(bis(trifluoromethylsulfonyl)imide)) (FK209) were obtained from Xi'an Polymer Light Technology Corp. Toluene (TL, 99% (AR)) was purchased from Beijing Chemical Works. Acetonitrile (ACN, ≥99.9% (HPLC)), 4-tert-butylpyridine (4-TBP, 96%), lithium bis(trifluoromethylsulfonyl)imide (LiTFSI), and acetonitrile (anhydrous, 99.8%) were obtained from Sigma-Aldrich.

Synthesis of PQDs:

$FAPbI_3$ PQDs were synthesized according to the literature with modifications.[1] Briefly, 0.78 g of FAAc and 15 mL of OA were added to a three-neck flask and evacuated under vacuum at room temperature for 1 hour. The solution was then heated to 120 °C under a nitrogen atmosphere, and after ~30 min, the FA-OA precursor was obtained. The solution was cooled to 80 °C and kept at this temperature until further use. In another three-neck flask, 0.688 g of PbI_2, 40 mL of ODE, 8 mL of OA, and 4 mL of OAm were added and evacuated under vacuum at 120 °C for 30 min until the solution became

clear. The solution was then cooled to 80 °C. Then, the FA-OA precursor was swiftly injected into the PbI_2 precursor. After ~5 s, the mixture was cooled in an ice bath.

Purification of PQDs:

The purification process is mainly divided into two steps. In the first step, 36 mL of 2-pentanol was added to the crude PQDs solution to remove excess species and wash off some ligands on the surface of PQDs. The solution was then centrifuged at 8000 rpm for 5 min, and the supernatant was discarded. The PQDs were then redispersed in a mixture of n-hexane and toluene (with a volume ratio of 4:1). It has been reported that toluene shows better solubility for PQDs, while hexane provides better stability for the quantum dots, and therefore a mixture of n-hexane and toluene was used here. FAI and 3-CF_3-PTAI were separately dissolved in acetonitrile solvent to obtain FAI solution (1 mg/mL) and 3-CF_3-PTAI solution (1 mg/mL). These solutions are then mixed in different ratios to obtain the 3-CF_3-PTAI/FAI solutions.

In the second step, pure acetonitrile, FAI solution, and different mass ratios of 3-CF_3-PTAI/FAI solution were added to the PQD solution as an antisolvent (with an antisolvent to solvent volume ratio of 5:1). After thorough and uniform mixing, the solution was centrifuged at 8000 rpm for 5 min. The resulting solid deposit was dissolved in n-hexane and centrifuged at 4000 rpm for 5 min to remove residual salts and aggregated PQDs. Before device fabrication, the PQD solution was concentrated to ~70 mg/mL in n-octane.

Fabrication of PQDSCs:

The ITO glass substrate underwent a cleaning process involving sequential ultrasonication in deionized water, acetone, and ethanol. Subsequently, the ITO substrate was exposed to ultraviolet-ozone treatment for 20 min. The SnO_2 nanoparticle solution was diluted with deionized water (2.67%), which was subsequently spin-coated onto the ITO substrate at a speed of 4000 rpm for 30 s. The sample was then sintered at 150 °C for 30 min under ambient conditions. Before depositing the PQD solid film, the SnO_2 film was subjected to ultraviolet-ozone treatment for 15 min. The ligand solution was prepared by dissolving MAI in the MeOAc with the sonication for

~20 min and excess salts were removed through centrifugation at 4000 rpm for 5 min. The PQD solution with a concentration of ~70 mg/mL in octane was spin-coated onto the SnO_2 film. The spin-coating process consisted of two steps: first, at 1000 rpm for 10 seconds, and then at 2000 rpm for 20 s. Subsequently, the PQD solid film was briefly immersed in the ligand solution for 3-5 s, followed by rinsing with MeOAc. This process was repeated 3-4 times to achieve the PQD solid film with a thickness of ~400 nm. The deposition of the PQD solid film was conducted under ambient conditions with a humidity of 20-30%. The hole transport layer was then spin-coated onto the PQD solid film at 4000 rpm for 30 s, using a solution composed of 72.3 mg of Spiro-OMeTAD, 28.8 μL of 4-TBP, 17.5 μL of bis(trifluoromethane) sulfonamide lithium salt (Li-TFSI) stock solution (520 mg/mL in acetonitrile), 10 μL of Co-complex (FK209) stock solution (300 mg/mL in acetonitrile), and 1 mL of chlorobenzene. Finally, an Ag electrode with a thickness of 80 nm was deposited onto the Spiro-OMeTAD layer through thermal evaporation.

Material characterization:

The transmission electron microscope (JSM 2100) was utilized to collect TEM images at an accelerating voltage of 200 kV. A scanning electron microscope (JEOL-7500) was employed to measure SEM images at an accelerating voltage of 3 kV. Fourier Transform Infrared Spectroscopy (FTIR) spectrum was measured using Nicolet 6700 Fourier Transform Infrared Spectrometer in transmittance mode, and the PQD solid film was deposited on a CaF_2 glass for the measurement. Ocean MAYA2000PRO spectrometer and Fluorolog spectrophotometer (HORIBA JOBIN YVON) were used to measure light absorption and PL spectra with an excitation of 550 nm. XRD patterns were measured using Rigaku D/max2500 with Cu Ka radiation (λ = 1.54178 Å). GIWAXS and GISAXS patterns were obtained using Xeuss 3.0 HR with Mo Ka radiation (λ = 1.54189 Å). XPS spectra were obtained with a Thermo Scientific Escalab 250Xi US equipped with a micro-focus monochromatic Al Kα X-ray source. The instrument resolution was determined to be 0.45 eV based on the Ag 3d5/2 peak. The atomic force microscope (AFM) used for measuring AFM images and film roughness

was the ICON model from Veeco/Bruker.

Photovoltaic performance measurement:

The *J-V* curve was recorded using a Keithley 2400 digital source meter, while the AAA-class solar simulator (Enlil SS-F5-3A) provided AM1.5G illumination with a light intensity of 100 mW/cm^2. Before the *J-V* measurement, the light intensity was calibrated using a certified reference Si solar cell (Fraunhofer ISE). The test was conducted under nitrogen protection. The working area of the solar cell was 0.04 cm^2 and was defined using a black metallic mask. For incident photon-to-electron conversion efficiency (IPCE) spectrum measurements, an Enli Technology QE-R system was used, which consisted of a xenon lamp (QE-LD), a Czerny-Turner monochromator (QE-M110), an optical imaging system, and a light intensity detection system (QE-M1). Before the measurement, the setup was calibrated using a certified reference silicon solar cell (SRC 2020). Transient photovoltage (TPV) and transient photocurrent (TPC) of PQDSCs were recorded using the Zahner Xenium C-Pro electrochemical workstation.

Theoretical Calculations:

The Vienna Ab initio Simulation Package (VASP) was utilized for conducting first-principles calculations[2]. The electron-ion interaction was described using the projected-augmented-wave (PAW) method, while Grimme's DFT-D3 was applied for dispersion correction. All calculations employed a plane-wave basis set with an energy cutoff of 400 eV. To model the FA-I surfaces, a slab with 3×3 periodicity in the a-b plane and a 15 Å vacuum along the c-axis was utilized. The surface structure of both the PQD and the molecule was optimized until the forces were below 0.05 eV/Å and the energy below 1.0×10^{-5} eV. For the Brillouin zone, a Monk Horst-Pack k-point mesh of (2×2×1) was adopted.

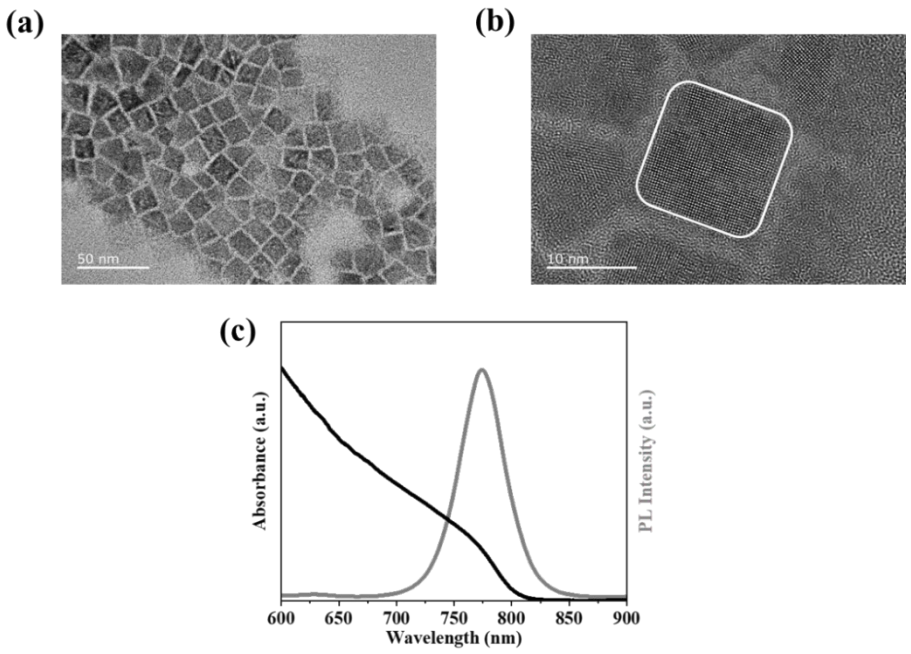

Fig. S1 (a) Transmission electron microscopy, (b) high-resolution transmission electron microscopy images and (c) light absorption and PL spectra of PQDs synthesized using the hot injection method.

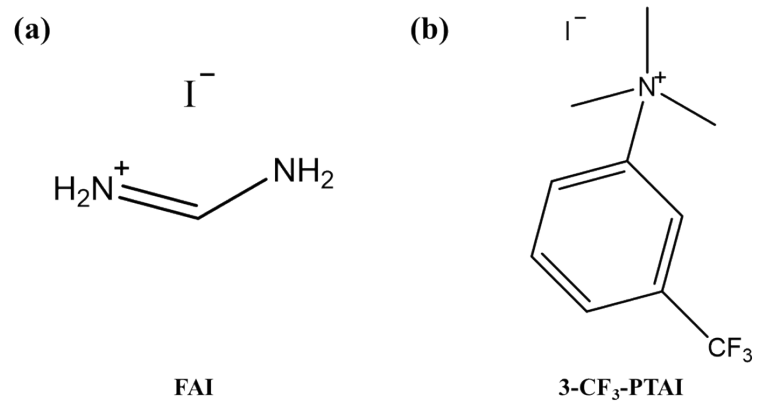

Fig. S2 Molecular structures of (a) FAI and (b) 3-CF_3-PTAI.

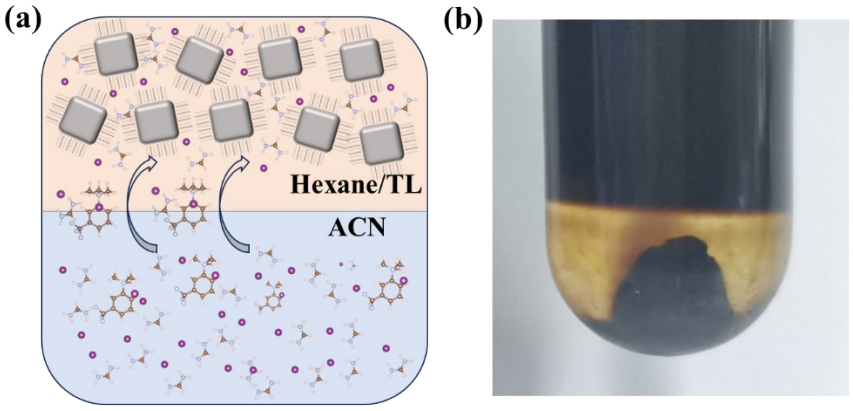

Fig. S3 (a) Schematic diagram and (b) photograph of the PQD solution during the PTC treatment.

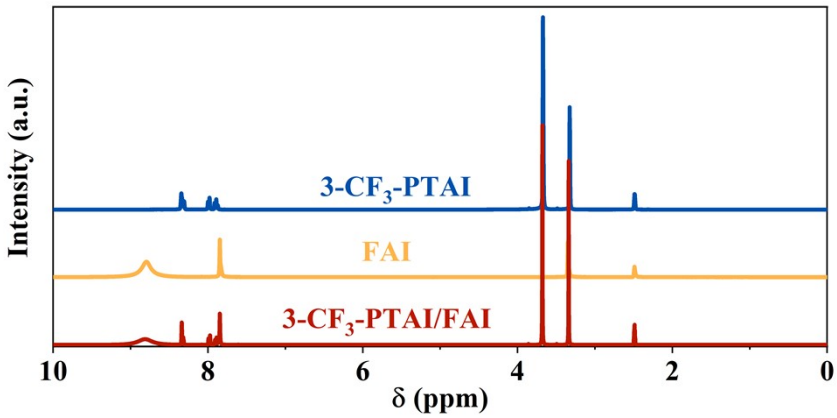

Fig. S4 Overview NMR spectra of 3-CF_3-PTAI, FAI and 3-CF_3-PTAI/FAI system

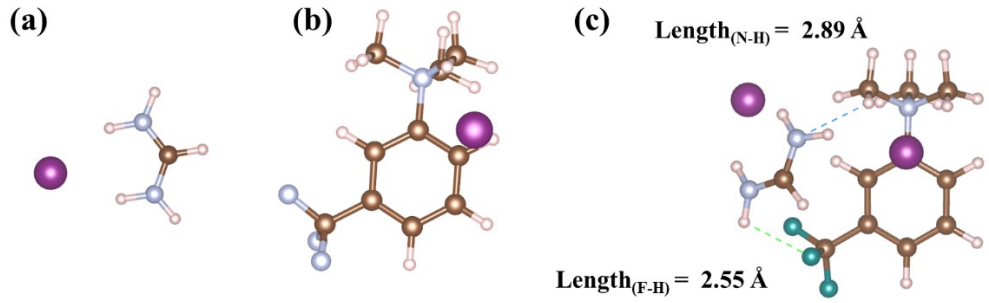

Fig. S5 Optimized configurations of (a) FAI, (b) 3-CF_3-PTAI and (c) 3-CF_3-PTAI/FAI system, which indicates that the hydrogen bonds could be formed between the FAI and 3-CF_3-PTAI molecules.

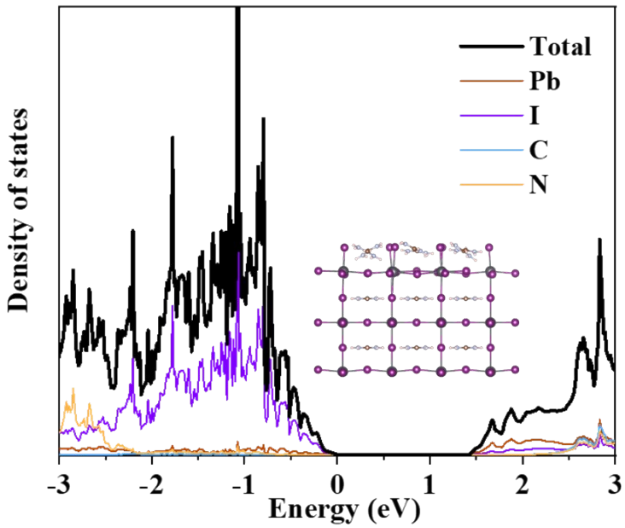

Fig. S6 DOS curves of the PQD passivated by FAI molecule. The inset depicts the corresponding optimization structure.

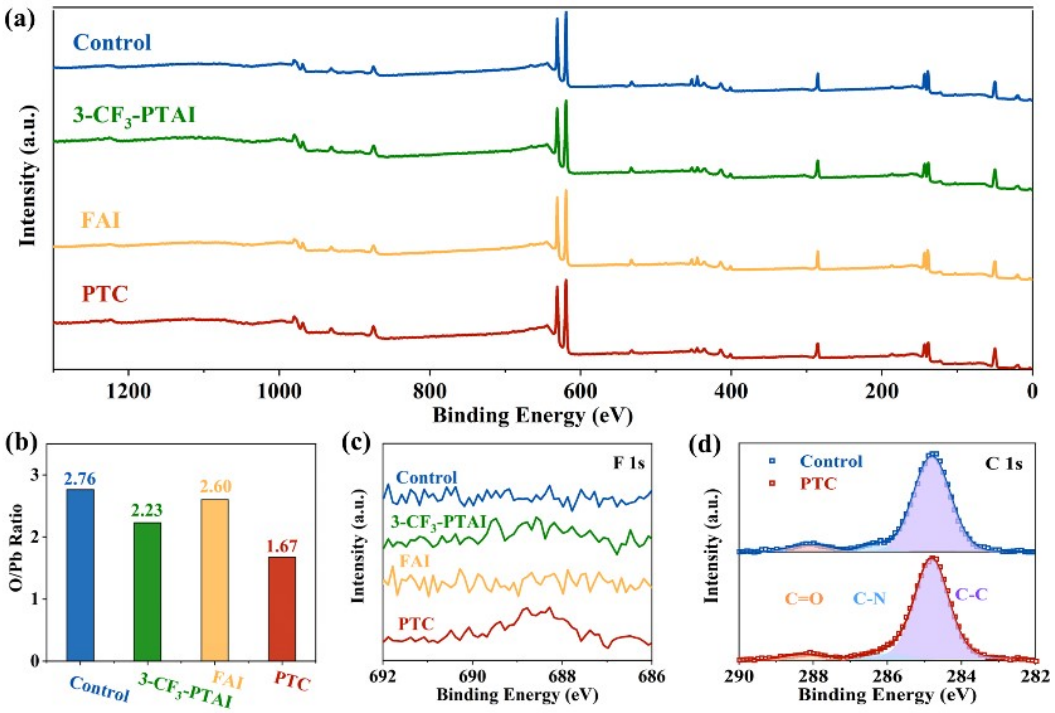

Fig. S7 (a) Overview XPS spectra, (b) O/Pb ratio, (c) core level XPS spectra of F 1s of PQDs. (d) Core level XPS spectra of C 1s of control and PTC-based PQDs.

In Fig. S7d, the peaks located at 288.10, 285.91 and 284.77 eV correspond to the C=O, C-N and C-C bonds, respectively, among which the peaks at 288.10 and 284.77 eV are attributed to OA/OAM ligands.[3, 4] The C=O signal peak of PTC-based PQDs is significantly reduced compared to control PQDs, indicating decreased OA ligands on the surface of PTC-PQDs.

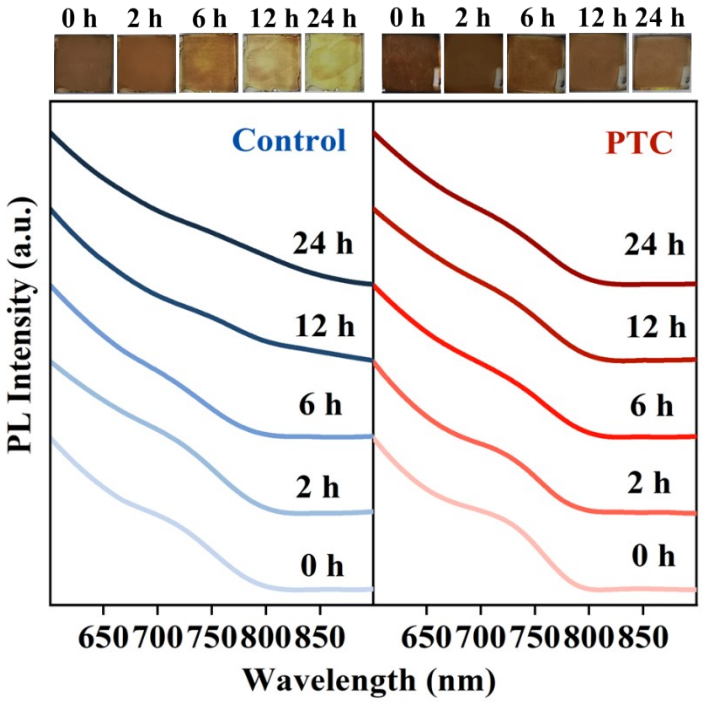

Fig. S8 The light absorption spectra of control and PTC-based PQD solid films with aging for 24 hours in an environment condition with a humidity of 50±5% and annealing at 80°C. The insets show the photographs of the control and PTC-based PQD solid films.

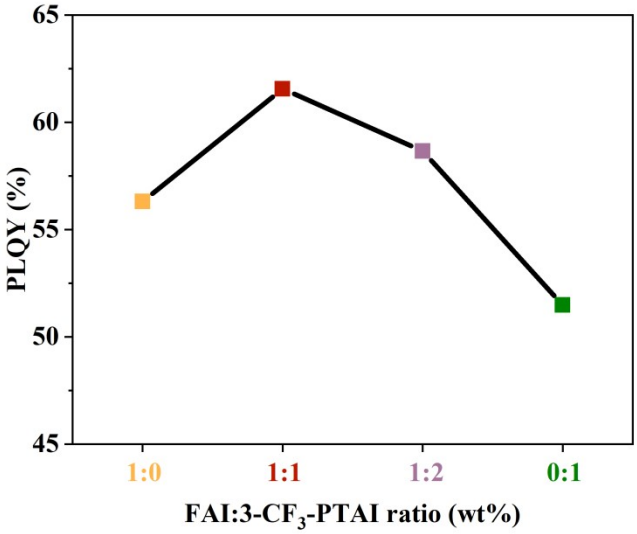

Fig. S9 PLQY values of the PTC-based PQDs as a function of the ratio of the FAI to 3-CF_3-PTAI molecules during the PTC treatment of PQDs.

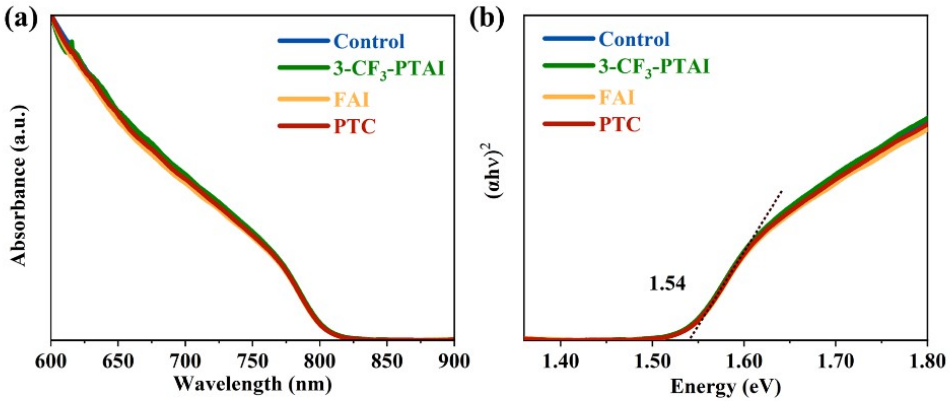

Fig. S10 (a) Light absorption spectra and (b) tauc plots of PQDs.

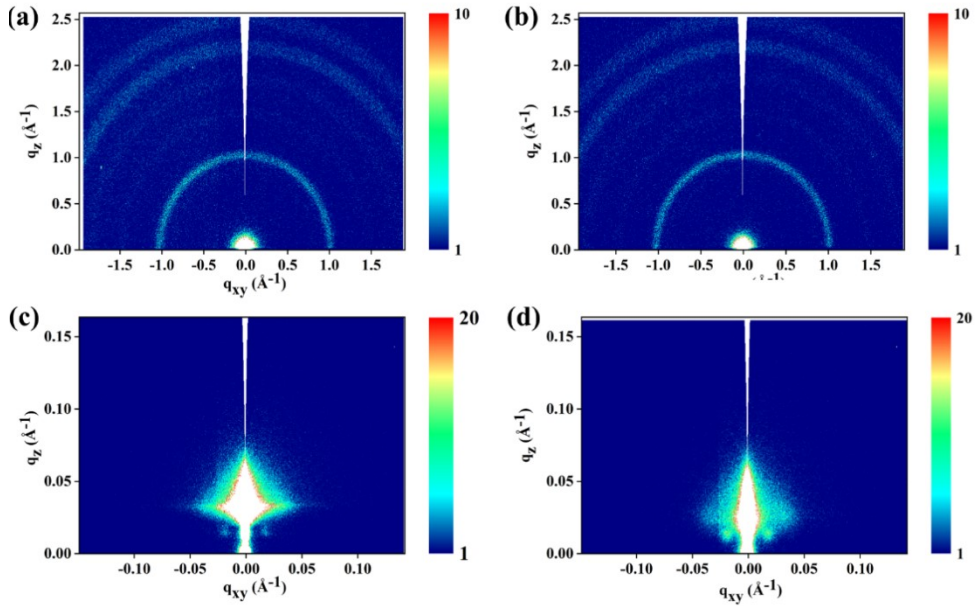

Fig. S11 2D GIWAXS of (a) 3-CF_3-PTAI- and (b) FAI-based PQD solids. 2D GISAXS patterns of (c) 3-CF_3-PTAI- and (d) FAI-based PQD solids.

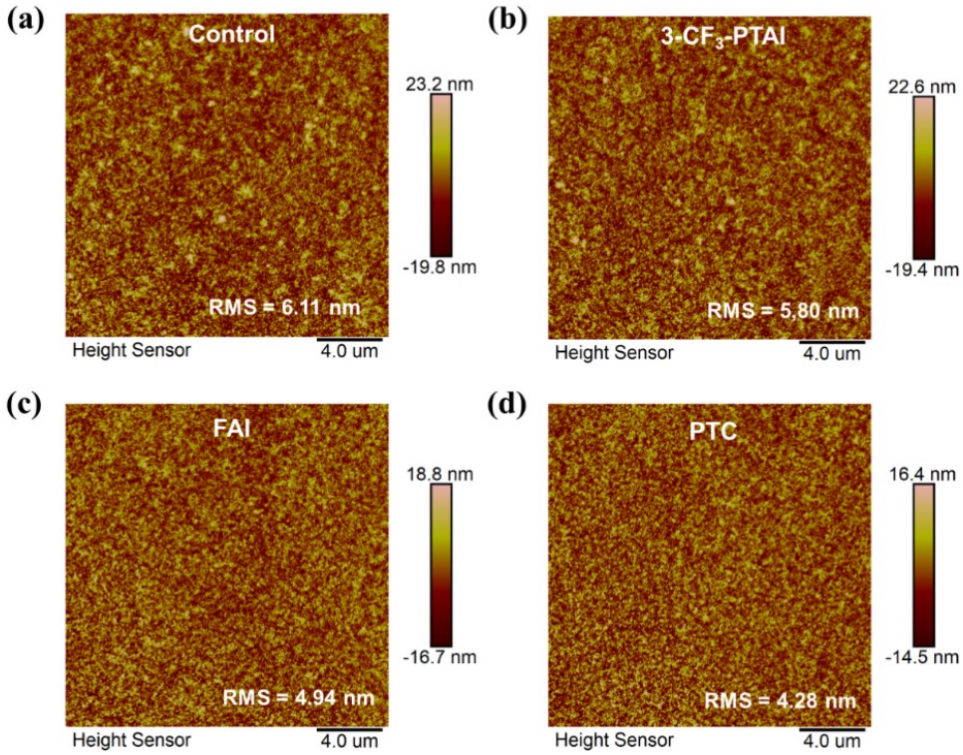

Fig. S12 AFM surface topography of (a) control, (b) 3-CF_3-PTAI-, (c) FAI- and (d) PTC-based PQD solid films

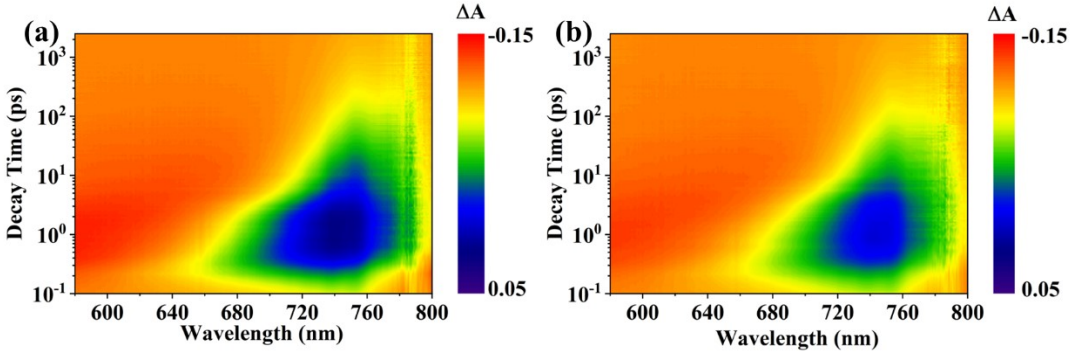

Fig. S13 2D pseudo-color fs-TA plots of (a) 3-CF_3-PTAI- and (b) FAI-based PQD solids.

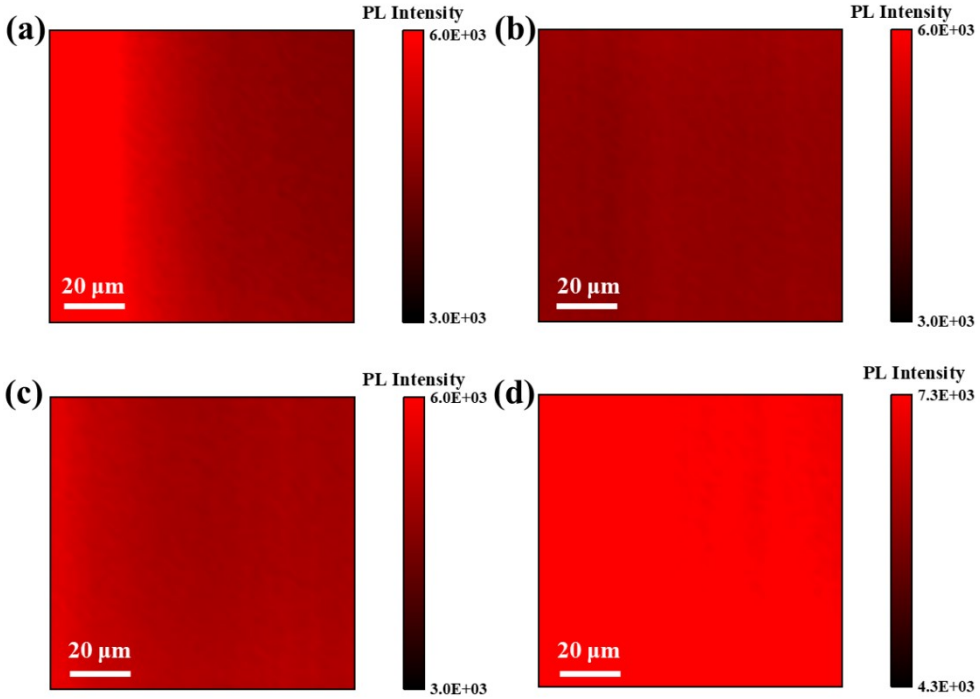

Fig. S14 PL mapping images of (a) control, (b) 3-CF_3-PTAI-, (c) FAI- and (d) PTC-based PQD solid films.

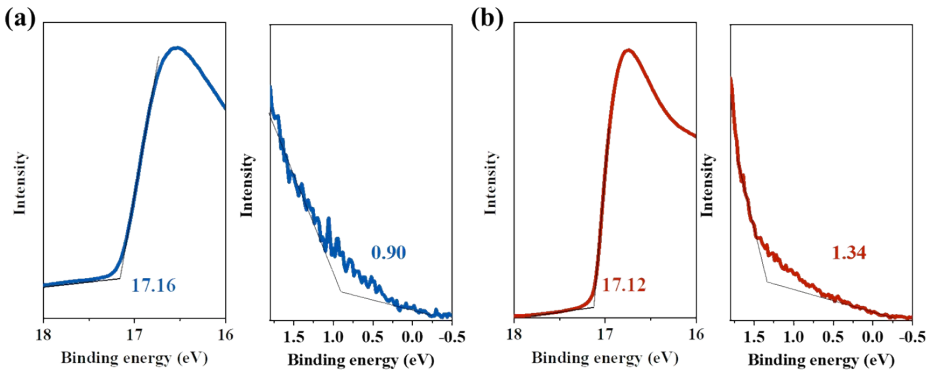

Fig. S15 UPS plots of (a) control and (b) PTC-based PQDs. Left and right figures show the the secondary electron cut-off region and valence band region, respectively.

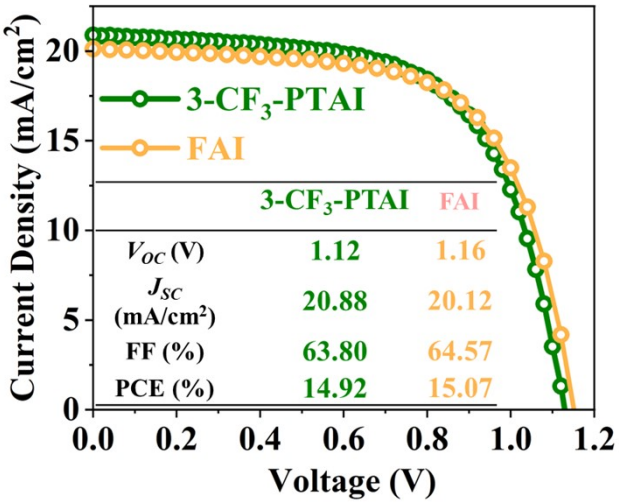

Fig. S16 *J-V* curves of 3-CF_3-PTAI- and FAI-based PQDSCs.

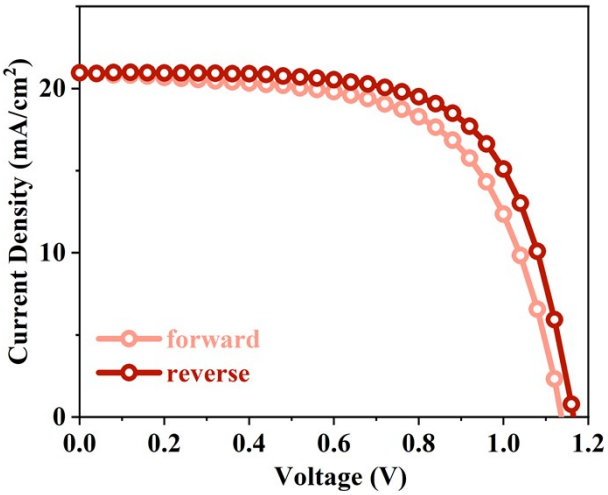

Fig. S17 *J-V* curves of the PTC-based PQDSC measured under reverse (from V_{OC} to J_{SC}) and forward voltage scanning (from J_{SC} to V_{OC}) directions.

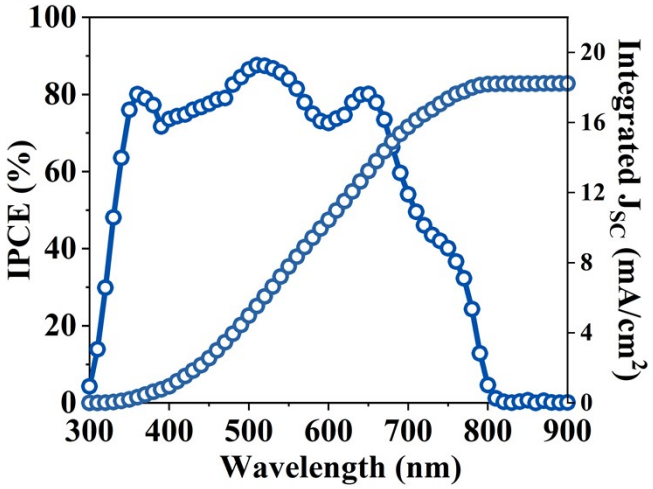

Fig. S18 IPCE spectrum of the control PQDSC.

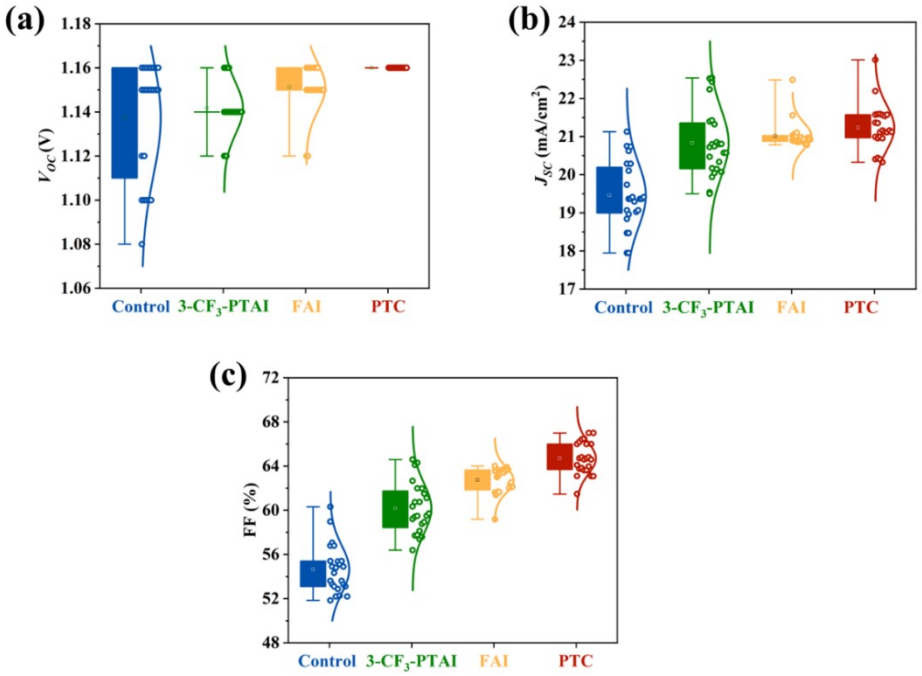

Fig. S19 Statistical (a) V_{OC}, (b) J_{SC} and (c) FF of control, 3-CF_3-PTAI-, FAI- and PTC-based PQDSCs. 24 devices fabricated from different batches were applied for statistics.

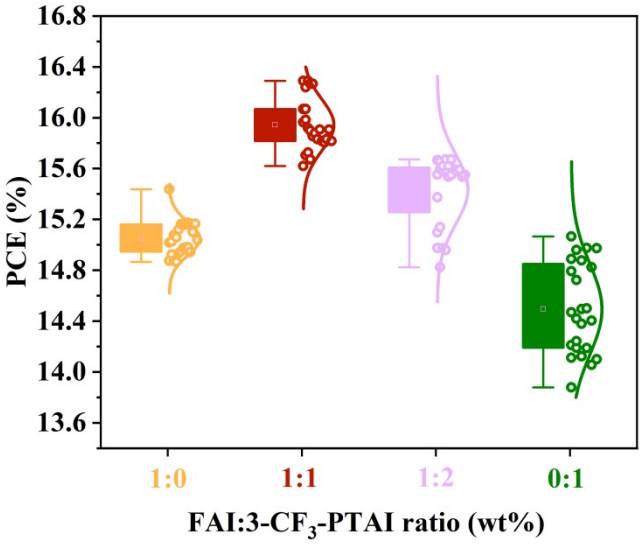

Fig. S20 Statistical PCE of the PQDSCs prepared by adjusting the mass ratio of FAI to 3-CF_3-PTAI for the PTC treatment of PQDs.

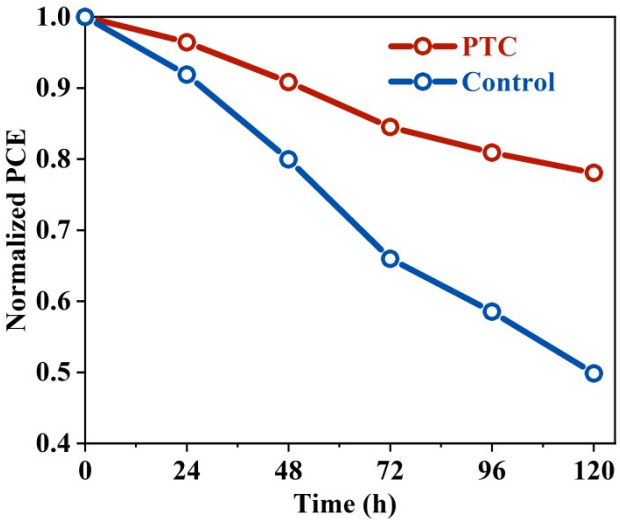

Fig. S21 Stabilities of unencapsulated control and PTC-based PQDSCs under continuous illumination at 100 mW/cm^2.

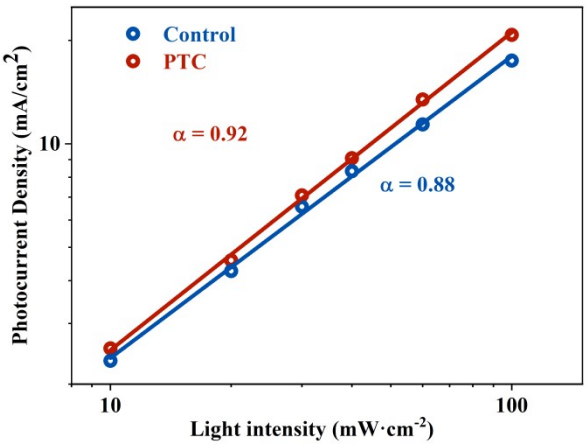

Fig. S22 Light intensity-dependent J_{SC} plots of control and PTC-based PQDSCs.

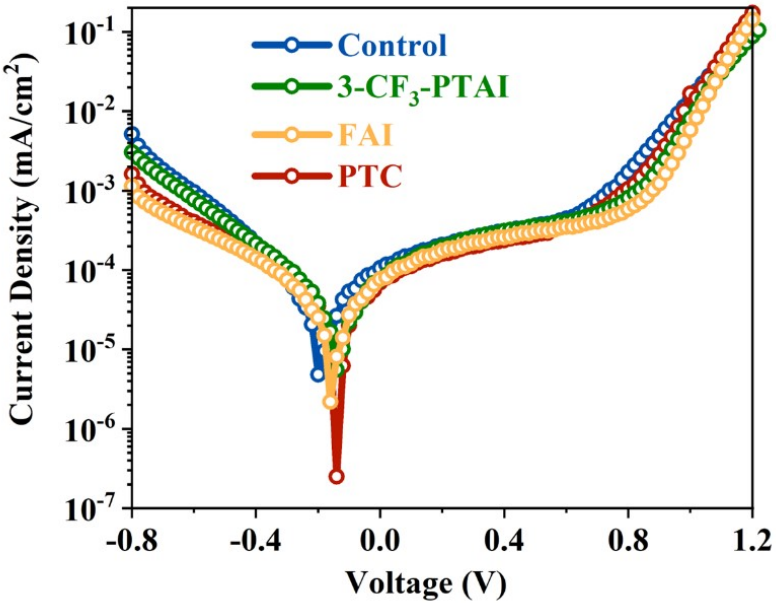

Fig. S23 Dark current curves of PQDSCs.

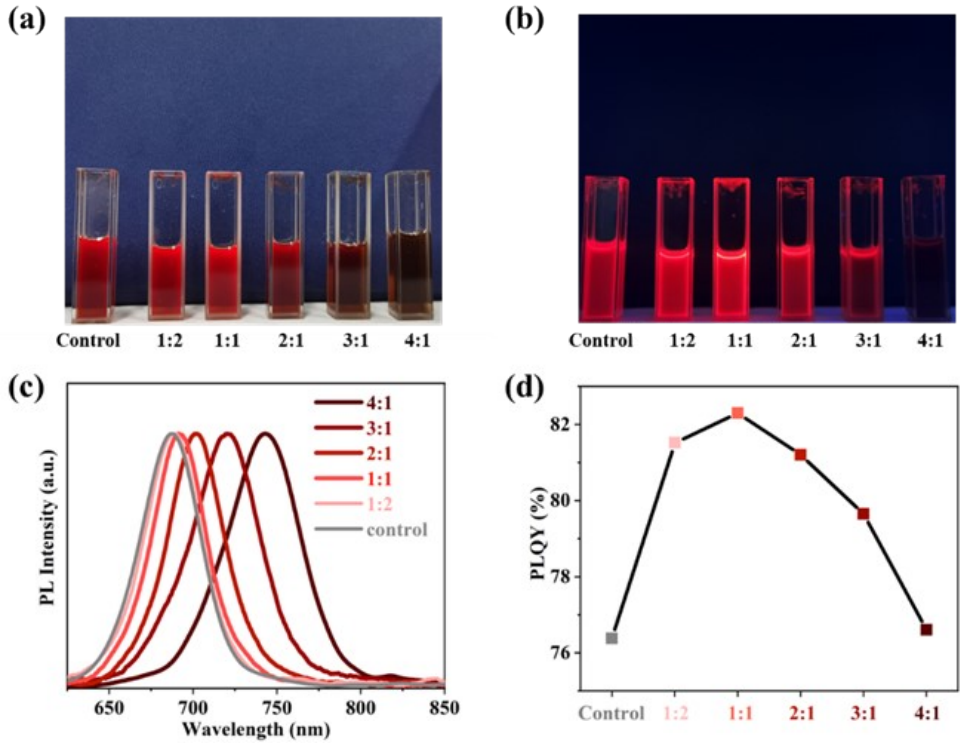

Fig. S24 Photographs of $CsPbI_3$ PQD solution under (a) natural light and (b) ultraviolet light. (c) Steady-PL spectra and (d) PLQY values of the $CsPbI_3$ PQDs with different ratios of FAI to 3-CF_3-PTAI for the PTC treatment.

Note S1: Universality of the phase transfer catalysis strategy

Based on the improved optoelectronic properties in $FAPbI_3$ PQDs using the PCT method, we also investigated such a method for inorganic $CsPbI_3$ PQDs. The $CsPbI_3$ PQD was treated using different different ratios of FAI to 3-CF_3-PTAI. **Fig. S24a** and **S24b** show the photographs of the $CsPbI_3$ PQD solution under natural light and ultraviolet light (365 nm), respectively, which reveals that the $CsPbI_3$ PQDs show improved photoluminescence under ultraviolet illumination, likely due to the defective surface matrix of $CsPbI_3$ PQDs was renovated. **Fig. S24c** and **S24d** display the normalized PL curves and PLQY values of $CsPbI_3$ PQDs. It can be seen that the PL peaks of the PQDs shift to the longer wavelength, which could be attributed to part of FA^+ penetrating into the $CsPbI_3$ PQDs forming $FA_xCs_{1-x}PbI_3$ PQDs. Meanwhile, the PLQY of $CsPbI_3$ PQDs was improved to 82.30% from 76.38%. The enhanced PLQY may result from the Cs^+ and I^- vacancies at the defective surface matrix of PQDs effectively filled during the PCT treatment, as demonstrated for $FAPbI_3$ PQDs. Therefore, the proposed PTC method could also be feasible for $CsPbI_3$ PQDs. Meanwhile, this work may also provide a potential method for the preparation of $FA_xCs_{1-x}PbI_3$ PQDs.

Table S1. Fitted parameters of the TRPL decay of PQDs.

Sample	A_1	τ_1 (ns)	A_2	τ_2 (ns)	τ_{ave} (ns)
Control	237596.94	7.47	2759.12	33.48	8.76
3-CF_3-PTAI	102722.21	8.89	1807.07	49.00	12.44
FAI	63856.84	10.01	1808.99	46.67	14.29
PTC	16580.83	15.18	1214.58	70.92	29.39

The PL decay curve decay was fitted using the following equation,[5]

$$I = A_1 \cdot exp\left(-\frac{t}{\tau_1}\right) + A_2 \cdot exp\left(-\frac{t}{\tau_2}\right) + A_0 \quad \text{（Eq. 1）}$$

where I is normalized PL intensity, A_1, A_2, and A_0 are constants, t is PL probe intensity decay time, τ_1 and τ_2 are fitted lifetimes. The average lifetime (τ_{ave}) was calculated using the following equation,

$$\tau_{ave} = \frac{A_1{\tau_1}^2 + A_2{\tau_2}^2}{A_1\tau_1 + A_2\tau_2} \quad \text{（Eq. 2）}$$

Table S2. Fitted parameters of the TAS delay of control and PTC-based PQD solids.

Sample	A_1	τ_1 (ps)	A_2	τ_2 (ps)	A_3	τ_3 (ps)	τ_{ave} (ps)
Control	0.62	7.62	0.30	61.06	0.11	567.06	437.17
PTC	0.83	5.27	0.33	67.21	0.13	605.67	469.41

The TAS decay curve was fitted using the following equation,[6]

$$f(t) = A_1 \cdot \exp\left(-\frac{t}{\tau_1}\right) + A_2 \cdot \exp\left(-\frac{t}{\tau_2}\right) + A_3 \cdot exp\left(-\frac{t}{\tau_3}\right) + A_0 \quad \text{（Eq. 3）}$$

where A_1, A_2, A_3 and A_0 are constants, t is decay time, τ_1, τ_2 and τ_3 are the fitted lifetimes of the hot-phonon bottleneck, Auger recombination, and trap-assisted quenching processes, respectively. The average lifetime (τ_{ave}) was calculated using the following equation,

$$\tau_{ave} = \frac{A_1{\tau_1}^2 + A_2{\tau_2}^2 + A_3{\tau_3}^2}{A_1\tau_1 + A_2\tau_2 + A_3\tau_3} \quad \text{（Eq. 4）}$$

Table S3. Summary of the photovoltaic parameters of $FAPbI_3$ PQDSCs.

Year	Cell stack	V_{oc} (V)	J_{sc} (mA/cm^2)	FF	PCE (%)	Ref.
2018	ITO/SnO_2/$FAPbI_3$ PQDs/Spiro-OMeTAD/Au	1.1	11.83	0.64	8.38	[1]
2018	FTO/TiO_2/ $FAPbI_3$ PQDs/Spiro-OMeTAD/MoO_X/Al	1.12	11.85	0.68	9.01	[7]
2019	FTO/TiO_2/ $FAPbI_3$ PQDs/Spiro-OMeTAD/MoO_X/Al	1.15	14.99	0.66	11.43	[8]
2019	FTO/TiO_2/ $FAPbI_3$ PQDs/Spiro-OMeTAD/MoO_X/Al	1.09	13.61	0.8	11.96	[9]
2019	FTO/TiO_2/ $FAPbI_3$ PQDs/PTAA/MoO_x/Al	1.15	15.97	0.66	12	[10]
2019	ITO/SnO_2/$FAPbI_3$ PQDs/Spiro-OMeTAD/Ag	1.1	15.4	0.74	12.7	[11]
2020	FTO/TiO_2/ $FAPbI_3$ PQDs/PTAA/MoO_X/Ag	1.14	16.02	0.7	12.78	[12]
2020	FTO/TiO_2/ $FAPbI_3$ PQDs/polymer/PTAA/MoO_X/Ag	1.12	16.7	0.71	13.2	[13]
2022	ITO/PEDOT: PSS/ $FAPbI_3$ PQDs/PCBM/BCP/Ag	0.89	14.56	0.78	10.13	[14]
2022	FTO/TiO_2/ $FAPbI_3$ PQDs/PTAA/MoO_X/Ag	1.18	15.63	0.64	11.93	[15]
2022	FTO/TiO_2/ $FAPbI_3$ PQDs/PTAA/MoO_X/Ag	1.15	18.45	0.68	14.47	[3]
2022	ITO/SnO_2/$FAPbI_3$ PQDs/Spiro-OMeTAD/Au	1.12	18.5	0.67	13.8	[16]
2022	FTO/TiO_2/ $FAPbI_3$ PQDs/PTAA/MoO_X/Ag	1.14	17.3	0.76	15.1	[4]
2023	ITO/SnO_2/$FAPbI_3$ PQDs/Spiro-OMeTAD/Au	1.15	18.03	0.73	15.34	[17]
2023	**ITO/SnO_2/$FAPbI_3$ PQDs/Spiro-OMeTAD/Ag**	**1.16**	**20.95**	**0.67**	**16.29**	**This work**

Table S4. Fitted V_{OC} decay signals of control and PTC-based PQDSCs.

Samples	A_1	$\tau_1\,(ms)$	A_2	$\tau_2\,(ms)$	$\tau_{ave}\,(ms)$
Control	0.55	0.11	0.29	1.68	1.5
PTC	0.40	0.27	0.46	2.70	2.5

The V_{OC} decay was fitted using the following equation,[6]

$$V_{OC} = A_1 \cdot exp\left(-\frac{t}{\tau_1}\right) + A_2 \cdot exp\left(-\frac{t}{\tau_2}\right) + A_0 \quad \text{(Eq. 5)}$$

where A_1, A_2, and A_0 are constants, t is V_{OC} decay time, τ_1 and τ_2 are fitted lifetimes. The τ_{ave} was calculated using the following equation,

$$\tau_{ave} = \frac{A_1{\tau_1}^2 + A_2{\tau_2}^2}{A_1\tau_1 + A_2\tau_2} \quad \text{(Eq. 6)}$$

Table S5. Fitted J_{SC} decay signals of control and PTC-based PQDSCs.

Samples	A_1	$\tau_1\ (\mu s)$	A_0
Control	0.69	35.61	0.08
PTC	1.26	15.33	0.03

The J_{SC} decay was fitted using the following equation,[5]

$$V_{OC} = A_1 \cdot exp\left(-\frac{t}{\tau_1}\right) + A_0 \qquad \text{(Eq. 7)}$$

where A_1 and A_0 are constants, t is decay time, τ_1 is fitted lifetimes.

1. J. Xue, J.-W. Lee, Z. Dai, R. Wang, S. Nuryyeva, M. E. Liao, S.-Y. Chang, L. Meng, D. Meng, P. Sun, O. Lin, M. S. Goorsky and Y. Yang, *Joule*, 2018, **2**, 1866-1878.
2. Y. Wang, X. Mei, J. Qiu, Q. Zhou, D. Jia, M. Yu, J. Liu and X. Zhang, *J. Phys. Chem. Lett.* , 2021, **12**, 11330-11338.
3. X. Zhang, H. Huang, L. Jin, C. Wen, Q. Zhao, C. Zhao, J. Guo, C. Cheng, H. Wang, L. Zhang, Y. Li, Y. M. Maung, J. Yuan and W. Ma, *Angew. Chem. Int. Ed.*, 2022, **14**, 241.
4. F. Li, X. Zhang, J. Shi, L. Jin, J. Qiao, J. Guo, H. Yin, Y. Li, J. Yuan and W. Ma, *Adv. Funct. Mater.*, 2023, **33**, 2302542.
5. Q. Zhou, J. Qiu, Y. Wang, M. Yu, J. Liu and X. Zhang, *ACS Energy Lett.*, 2021, **6**, 1596-1606.
6. D. Jia, J. Chen, S. Zheng, D. Phuyal, M. Yu, L. Tian, J. Liu, O. Karis, H. Rensmo, E. M. J. Johansson and X. Zhang, *Adv. Energy Mater.*, 2019, **9**, 1902809.
7. A. Hazarika, Q. Zhao, E. A. Gaulding, J. A. Christians, B. Dou, A. R. Marshall, T. Moot, J. J. Berry, J. C. Johnson and J. M. Luther, *ACS Nano*, 2018, **12**, 10327-10337.
8. Q. Zhao, A. Hazarika, X. Chen, S. P. Harvey, B. W. Larson, G. R. Teeter, J. Liu, T. Song, C. Xiao, L. Shaw, M. Zhang, G. Li, M. C. Beard and J. M. Luther, *Nat. Commun.*, 2019, **10**, 2842.
9. M. Suri, A. Hazarika, B. W. Larson, Q. Zhao, M. Vallés-Pelarda, T. D. Siegler, M. K. Abney, A. J. Ferguson, B. A. Korgel and J. M. Luther, *ACS Energy Lett.*, 2019, **4**, 1954-1960.
10. F. Li, S. Zhou, J. Yuan, C. Qin, Y. Yang, J. Shi, X. Ling, Y. Li and W. Ma, *ACS Energy Lett.*, 2019, **4**, 2571-2578.
11. J. Xue, R. Wang, L. Chen, S. Nuryyeva, T. H. Han, T. Huang, S. Tan, J. Zhu, M. Wang, Z. K. Wang, C. Zhang, J. W. Lee and Y. Yang, *Adv. Mater*, 2019, **31**, 1900111.
12. X. Ling, J. Yuan, X. Zhang, Y. Qian, S. M. Zakeeruddin, B. W. Larson, Q. Zhao, J. Shi, J. Yang, K. Ji, Y. Zhang, Y. Wang, C. Zhang, S. Duhm, J. M. Luther, M. Grätzel and W. Ma, *Adv. Mater*, 2020, **32**.
13. K. Ji, J. Yuan, F. Li, Y. Shi, X. Ling, X. Zhang, Y. Zhang, H. Lu, J. Yuan and W. Ma, *J. Mater. Chem. A*, 2020, **8**, 8104-8112.
14. Y. Xu, H. Li, S. Ramakrishnan, D. Song, Y. Zhang, M. Cotlet and Q. Yu, *ACS Appl. Energy Mater.*, 2022, **5**, 9858-9869.
15. C. Zhao, X. Zhang, H. Huang and J. Yuan, *J. Chem. Phys.*, 2022, **157**, 031101.
16. S. Ding, M. Hao, C. Fu, T. Lin, A. Baktash, P. Chen, D. He, C. Zhang, W. Chen, A. K. Whittaker, Y. Bai and L. Wang, *Adv. Sci.*, 2022, **9**, 2204476.
17. S. Ding, J. A. Steele, P. Chen, T. Lin, D. He, C. Zhang, X. Fan, E. Solano, A. K. Whittaker, M. Hao and L. Wang, *Adv. Energy Mater.*, 2023, **23**, 2301817.